

See discussions, stats, and author profiles for this publication at: <https://www.researchgate.net/publication/228658110>

Numerical Simulation of the Gas– Solid Flow in Three–Dimensional Pneumatic Conveying Bends

ARTICLE *in* INDUSTRIAL & ENGINEERING CHEMISTRY RESEARCH · SEPTEMBER 2008

Impact Factor: 2.59 · DOI: 10.1021/ie800108c

CITATIONS

31

READS

184

2 AUTHORS:



Kaiwei Chu

University of New South Wales

69 PUBLICATIONS 1,405 CITATIONS

SEE PROFILE



Aibing Yu

University of New South Wales

622 PUBLICATIONS 11,725 CITATIONS

SEE PROFILE

Numerical Simulation of the Gas–Solid Flow in Three-Dimensional Pneumatic Conveying Bends

K. W. Chu and A. B. Yu*

Laboratory for Simulation and Modeling of Particulate Systems, School of Materials Science and Engineering, University of New South Wales, Sydney, NSW 2052 Australia

The laden gas–solid flow in a pneumatic conveying bend is featured with intensive gas–solid, particle–particle, and particle–wall interactions, which are however difficult to quantify experimentally. In this work, these interactions are obtained by use of a three-dimensional combined continuum and discrete model. The model is achieved by combining our code for discrete element method for solid phase with the commercial software package Fluent for computational fluid dynamics for gas phase. The applicability of the approach is first qualitatively verified by comparing the simulated results with the observations in the literature in terms of typical flow features in bends such as roping, particle segregation, particle velocity reduction, particle recirculation, and pressure fluctuation. The gas–solid, particle–particle, and particle–wall interaction forces are then analyzed to understand their role in governing the complicated flow. It is found that the intensive gas–particle interaction at the outer wall makes the peak of the axial velocity shift from the outer wall to the inner wall of a pipe. Correspondingly, the so-called secondary flow is suppressed in the outer wall region but enhanced along the side wall. The spatial distribution of particle–wall interaction is obtained and shown to correspond to the wearing pattern in a bend. This distribution is also found in the particle–particle interaction close to the bend wall. Not only gas–solid interaction but also particle–particle interaction contributes to the dispersion of a rope. Finally, simulations are also conducted to investigate the effects of inlet conditions such as gas and solid flow rates on these interaction forces.

1. Introduction

Pneumatic conveying is widely used in process industries to transport granular materials of different types because of its cleanliness and flexibility of layout compared with mechanical conveying methods. Bends, which are one of the most common setups in a pneumatic conveying system, are known to be responsible for various problems such as high pressure loss, product segregation and degrading, roping, and pipe wear. In order to minimize those problems, there are different bend designs in practice, such as bends with different geometries, which can reduce erosion or avoid choking (e.g., T-bend, tubing bend, ankle-bend, and ribbed bend¹) and bends with flow mixers (e.g., nozzles, air jet injection, and swirl vanes) which aim to disperse ropes or reduce choking.² The success of such a design varies, partially because of the limited understanding of the limited internal flow. In the past, many experimental and numerical studies have been made to overcome the problem.^{3–11}

In recent years, numerical methods have been increasingly used to study gas–solid flow. The popular mathematical models proposed thus far can be grouped into two categories: the continuum approach at a macroscopic level represented by the two-fluid model (TFM), and the discrete approach at a microscopic level mainly represented by the so-called combined continuum and discrete model (CCDM).^{12–14} In TFM, both gas and solid phases are treated as interpenetrating continuum media in a computational cell that is much larger than individual particles but still small compared to the size of process equipment. This model is preferred in process modeling and applied research because of its computational convenience. However, its effective use depends heavily on the constitutive or closure relations, which are not generally available for solids at this stage of development. In CCDM, the motion of individual

particles is obtained by solving Newton's equations of motion while the flow of continuum gas is determined by computational fluid dynamics (CFD) on a computational cell scale.^{13–15} While the governing equations for gas phase are the same as those in TFM—a treatise that has been widely accepted in engineering research—its governing equations for solid flow are mainly based on the distinct element method (DEM).¹⁶ CCDM has been recognized as an effective method to study the fundamentals of particle–fluid two-phase flow, as briefly reviewed by various investigators.^{12,15,17} By means of a proper average method, DEM-based simulation can also generate information to support continuum modeling (see, for example, refs 18 and 19).

In the previous numerical studies of gas–solid flow in bends, mainly TFM and Lagrangian particle tracking (LPT) methods were used. In theory, LPT could be thought as a simplified model of CCDM, with the interaction between particles and the effect of particle phase on gas phase ignored. Because of that, the LPT model is applicable not to dense flow but to dilute flow. Tu and Fletcher⁶ used TFM to predict the mean streamwise velocity profiles of both the gas and particle phases and found that particle–wall interaction is the controlling factor in their case. Huber and Sommerfeld⁸ considered interparticle collisions and the reaction of particles on gas in their LPT model and found that interparticle collision contributes to the disintegration of rope. However, it appears that their model does not satisfactorily predict the shift of the region of high particle concentration from the outer wall to the middle of a bend. The same remark applies to the model developed by Yilmaz and Levy⁹ who used the concept of parcels instead of particles.

In general, the velocity vector for each phase can be divided into two components: the primary one in the axial direction and the secondary one normal to the pipe axis (or in the radial direction). The latter is referred to as the secondary flow. The role of the secondary flow in pneumatic conveying bends may be important. Levy and Mason⁷ showed that TFM can capture

* To whom correspondence should be addressed. Tel: 61-2-93854429. Fax: 61-2-93855956. E-mail: a.yu@unsw.edu.au.

the secondary flow of both gas and particle phases. They reported that gas and particle phases have a similar spatial velocity distribution. Akilli et al.²⁰ reported that the secondary flow can disperse a rope by carrying fine particles, and they also showed there is a radial particle size segregation by use of LPT method. The role of the secondary flow in rope dispersion was also reported in the LPT work by Yilmaz and Levy.⁹ These authors also found the LPT model is not able to predict that the quick dispersion of a rope in a sharp bend, which may involve strong particle–particle interactions.

CCDM has also been employed to study the gas–solid flow in pneumatic conveying in recent years.^{11,21–27} Some interesting findings have been reported. For example, Tsuji et al.¹⁴ obtained the plug flow pattern in a horizontal pneumatic conveying pipe. Li et al.²⁸ showed an intensive exchange of particles between the stationary layer (deposited particles) and the moving slug in a horizontal pipe both numerically and experimentally. Lim et al.¹¹ successfully reproduced different flow regimes observed under different operating conditions. Kuang et al.²⁷ recently examined the slug flow patterns in relation to the governing forces in horizontal pneumatic conveying. All these studies are limited to relatively simple systems, e.g., 2D simple geometry, flow conditions, or both. To date, no attempt has been made to study the gas–solid flow in bends.

In this work, a three-dimensional CCDM model is developed to simulate the gas–solid flow in pneumatic conveying bends. This is done by extending our previous CCDM code with Fluent as a platform, achieved by incorporating a DEM code into Fluent through its user defined functions (UDFs).²⁹ The approach is validated by the good agreement between simulated and measured results, quantitatively or qualitatively depending on the availability of data in the literature. On this basis, the interactions between gas and particles, between particles, and between particles and wall are analyzed in relation to the flow phenomena observed. Finally, the effects of gas and solid flow rates on these interaction forces in bends are also investigated.

2. Simulation Method

2.1. Mathematical Model. The CCDM model employed for this work is in principle the same as that used in our previous studies of the gas–solid flow in fluidized beds.^{13,15,29,30} As such, only a brief description of the model is given below.

The solid phase is treated as a discrete phase and described by a modified DEM, which incorporates a rolling friction model in the rotational equation of a particle.³¹ According to the model, the translational and rotational motions of a particle in a system at any time, t , caused by its interactions with neighboring particles or walls and surrounding gas under gravity, can be described by Newton's second law of motion:

$$m_i \frac{d\mathbf{V}_i}{dt} = m_i \mathbf{g} + \sum_{j=1}^{k_i} (\mathbf{f}_{cn,ij} + \mathbf{f}_{dn,ij} + \mathbf{f}_{ct,ij} + \mathbf{f}_{dt,ij}) + \mathbf{f}_{pf,i} \quad (1)$$

and

$$I_i \frac{d\boldsymbol{\omega}_i}{dt} = \sum_{j=1}^{k_i} (\mathbf{T}_{ij} + \mathbf{M}_{ij}) \quad (2)$$

where m_i , I_i , \mathbf{V}_i , and $\boldsymbol{\omega}_i$ are, respectively, the mass, moment of inertia, and translational and rotational velocities of particle i . The forces involved are the gravitational force, $m_i \mathbf{g}$, interparticle forces between particles i and j , which include the contact forces $\mathbf{f}_{cn,ij}$ and $\mathbf{f}_{ct,ij}$, and viscous damping forces $\mathbf{f}_{dn,ij}$ and $\mathbf{f}_{dt,ij}$, and the gas–particle interaction force, $\mathbf{f}_{pf,i}$. The interparticle forces are summed over the k_i particles in contact with particle i and depend on the normal and tangential deformations, δ_n and δ_t . Torques, \mathbf{T}_{ij} , are generated by tangential forces and cause particle i to rotate, because the interparticle forces act at the contact point between particles i and j and not at the particle center. \mathbf{M}_{ij} are the rolling friction torques that oppose the rotation of the i th particle. Table 1 lists the equations used to calculate the forces and torques considered in this work. For details and their justification, see refs 29 and 31–37.

The governing equations for gas phase are the same as those used in TFM. Two model formulations, referred to as models A and B, are available depending on the treatment of pressure.³⁸ Model A assumes that a pressure drop is shared between gas and solid phases, but model B assumes that the pressure applies to gas phase only. For monosized particles, both models can give reasonable results but model B is theoretically more acceptable for particle mixtures.¹⁵ Therefore, model B is used in this work, which considers particles of different sizes. Note that, in this model, the fluid drag force has implicitly included the pressure gradient force, a treatment that may limit its application but is valid for the gas–solid flow considered in this work. The governing equations are thus the conservations of mass and momentum in terms of the local mean variables over a computational cell, given by

$$\frac{\partial(\varepsilon)}{\partial t} + \nabla \cdot (\varepsilon \mathbf{u}) = 0 \quad (3)$$

and

$$\frac{\partial(\rho_f \varepsilon \mathbf{u})}{\partial t} + \nabla \cdot (\rho_f \varepsilon \mathbf{u} \mathbf{u}) = -\nabla P - \mathbf{F}_{fp} + \nabla \cdot (\varepsilon \boldsymbol{\tau}) + \rho_f \varepsilon \mathbf{g} \quad (4)$$

where ε , \mathbf{u} , t , ρ_f , P , \mathbf{F}_{fp} , $\boldsymbol{\tau}$, and \mathbf{g} are, respectively, porosity, fluid velocity and time, fluid density and pressure, volumetric fluid–particles interaction force, fluid viscous stress tensor, and gravity acceleration. $\mathbf{F}_{fp} = \sum_{i=1}^{k_c} \mathbf{f}_{pf,i}$, where k_c is the number of particles in a CFD cell. The turbulent flow of gas is described

Table 1. Components of Forces and Torques Acting on Particle i ^a

forces and torques		symbols	equations
normal forces	contact	$\mathbf{f}_{cn,ij}$	$-E/[3(1-\nu^2)](2R_i)^{1/2}\delta_n^{3/2}\mathbf{n}$
	damping	$\mathbf{f}_{dn,ij}$	$-c_n(3m_i E/[(2)^{1/2}(1-\nu^2)](R\delta_n)^{1/2})^{1/2}\mathbf{V}_{n,ij}$
tangential forces	contact	$\mathbf{f}_{ct,ij}$	$-\{\mu_s \mathbf{f}_{cn,ij}/ \boldsymbol{\delta}_t \}[1 - (1 - \min\{ \boldsymbol{\delta}_t , \boldsymbol{\delta}_{t,max}/\boldsymbol{\delta}_{t,max}\})^{3/2}]\boldsymbol{\delta}_t$
	damping	$\mathbf{f}_{dt,ij}$	$-c_t(6m_i \mu_s \mathbf{f}_{cn,ij})^{1/2}[(1 - \boldsymbol{\delta}_t/\boldsymbol{\delta}_{t,max})^{1/2}/\boldsymbol{\delta}_{t,max}]^{1/2}\mathbf{V}_{t,ij}$
torque	rolling	\mathbf{T}_{ij}	$\mathbf{R}_i \times (\mathbf{f}_{ct,ij} + \mathbf{f}_{dt,ij})$
	friction	\mathbf{M}_{ij}	$-\mu_r \mathbf{f}_{cn,ij} \hat{\boldsymbol{\omega}}$
body force	gravity	\mathbf{G}_i	$m_i \mathbf{g}$
particle–fluid interaction force		$\mathbf{f}_{pf,i}$	$(0.63 + \{4.8/(\text{Re}_{p,i})^{0.5}\}^2 \{\rho_f \mathbf{u}_i - \mathbf{V}_i\}(\mathbf{u}_i - \mathbf{V}_i)/2) \{\pi d_i^2/4\} \varepsilon_i^{-(\beta+1)}$

^a where $\mathbf{n} = \mathbf{R}_j/\mathbf{R}_i$, $\mathbf{V}_{ij} = \mathbf{V}_j - \mathbf{V}_i + \boldsymbol{\omega}_j \times \mathbf{R}_j - \boldsymbol{\omega}_i \times \mathbf{R}_i$, $\mathbf{V}_{n,ij} = (\mathbf{V}_{ij} \cdot \mathbf{n}) \cdot \mathbf{n}$, $\mathbf{V}_{t,ij} = (\mathbf{V}_{ij} \times \mathbf{n}) \times \mathbf{n}$, $\hat{\boldsymbol{\omega}} = \boldsymbol{\omega}/\omega_i$, $\{\text{Re}_{p,i}\} = \{\rho_f \varepsilon_i |\mathbf{u}_i - \mathbf{V}_i|/\mu_f\}$, $\beta = 3.7 - 0.65 \exp[-(1.5 - \log\{\text{Re}_{p,i}\})^2/2]$, $\varepsilon = 1 - \sum_{i=1}^N V_i/\Delta V_c$.

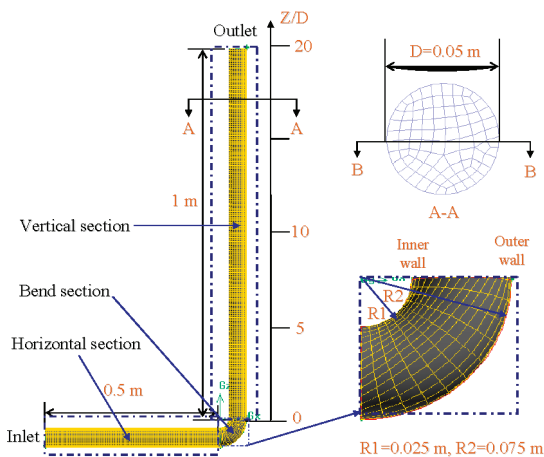


Figure 1. Schematic and numerical grid representation of the bend in the base case (cell volume varies from 3.513×10^{-8} to $6.170 \times 10^{-7} \text{ m}^3$).

by the standard k-epsilon two-equations turbulence model, although its effect on solid flow is ignored in this work.

The modeling of the solid flow by DEM is at the individual particle level, while the fluid flow by CFD is at the computational cell level. Their coupling is numerically achieved as follows. At each time step, DEM will give information, such as the positions and velocities of individual particles, for the evaluation of porosity and volumetric particle–fluid interaction force in a computational cell. CFD will then use these data to determine the gas flow field, which then yields the particle–fluid interaction forces acting on individual particles. Incorporation of the resulting forces into DEM will produce information about the motion of individual particles for the next time step. The fluid drag force acting on individual particles will react on the fluid phase from the particles, so that Newton's third law of motion is satisfied. In principle, time steps for gas and particle phases should be same. However, in some computation, the time step for gas phase can be larger than that of particle phase because gas flow is not so sensitive to the time step, and the treatment can improve computational efficiency. This treatment is adopted in the present work.

Our previous CCDM programs are all in-house codes. For complicated flow systems, the code development for the solution of fluid phase could be very time-consuming. On the other hand, commercial CFD software packages such as Fluent, CFX, and Star-CD are readily available for this purpose. So to take advantage of this CFD development, we have extended our CCDM code with Fluent as a platform, achieved by incorporating a DEM code into Fluent through its UDFs. The computational domain for particle and fluid phases is the same, with

Table 2. Parameters Used in the Base Case

phase	parameter	symbol	units	value
solid	mass flow rate		kg/s	31.1
	density	ρ	kg/m ³	1123
	particle radius	R_i	mm	1.4 ± 0.25
	rolling friction coefficient	μ_r	mm	0.005
	sliding friction coefficient	μ_s	(–)	0.3
	poisson's ratio	ν	(–)	0.3
	young's modulus	E	N/m ²	1×10^7
	damping coefficient	c	(–)	0.3
	time step	Δt	s	1×10^{-6}
	average particle velocity at inlet		m/s	7
gas	density	ρ	kg/m ³	1.225
	viscosity	μ	kg/m/s	1.8×10^{-5}
	velocity	V	m/s	11.9
	time step	Δt	s	1×10^{-5} to 1×10^{-3}

the boundary meshes automatically generated in Fluent for both phases. Consistent with the well-established treatments, at a boundary, nonslip condition applies to fluid phase, and the interaction between a particle and wall is determined in a way similar to the interparticle collision described above, with the wall assumed to be of infinitely large diameter. For convenience, the wall properties are simply assumed to be the same as those of particles in this work. The treatments have been widely used in the previous studies of particle–fluid flow.^{12–15,27–30,39}

2.2. Simulation Conditions. In this work, the gas–solid flow from a horizontal pipe to vertical pipe through a 90° bend is studied. For the purpose of model verification, the parameters used in the simulation are mainly taken from the experiments of Lee et al.¹⁰ As shown in Figure 1, the conveying pipe is 0.05 m in diameter and divided into three sections: horizontal, bend, and vertical. The length of the horizontal section is 0.5 m and that of the vertical section 1 m. The bend section consists of a 90° circular bend with an outer radius of 0.075 m and inner radius of 0.025 m. The whole bend was divided into 27 590 structured hexagonal grids. Trial simulations showed that finer grids do not result in any noticeable change in the simulation results.

In order to overcome the deficiency due to the shorter bend, the gas and solid velocity distribution at a fully developed flow section, measured by Tsuji and Morikawa,⁴⁰ is taken as the inlet condition in this work since the conditions in the two studies are comparable. The deduced velocity profiles of gas phase and solid concentration at the inlet from the experimental work by Tsuji and Morikawa are shown in Figure 3. From this figure it can be seen that the distributions of gas velocity and solid concentration are not uniform. The velocities of both phases at the top of the pipe are higher than those at the bottom, and the

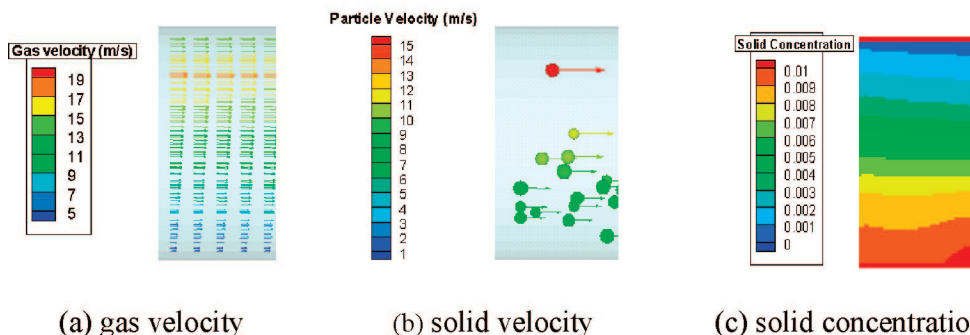


Figure 2. Conditions of gas and solid phases at the inlet of the horizontal section in the base case. Arrows represent velocity vectors, colored by the magnitudes in the axial direction in (a) and (b), and the sphere size in (b) represents particle size.

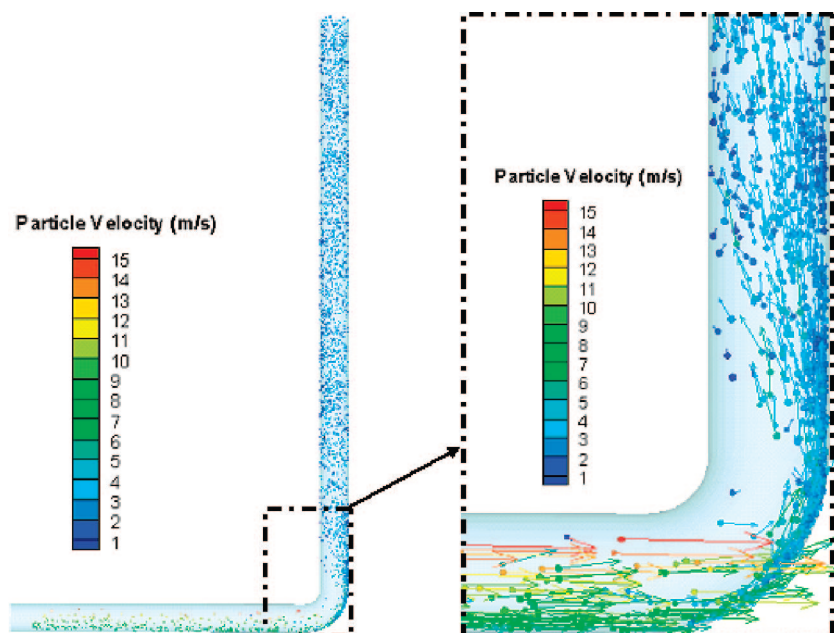


Figure 3. Simulated rope formation and dispersion, and particle velocity reduction in the model pipe when superficial gas velocity is 11.9 m/s. Arrows represent particle velocity vectors, and the spheres represent particle positions and sizes.

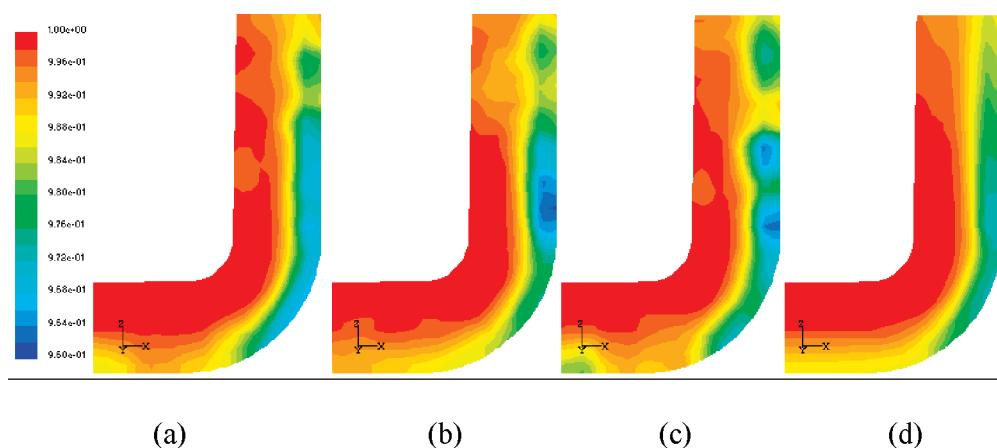


Figure 4. Spatial distribution of porosity ($1 - \text{solid concentration}$) at the bend at the B–B section (defined in Figure 18) for the base case at different times: (a) $t = 1.0$ s; (b) $t = 1.5$ s; (c) $t = 2$ s; (d) time-averaged over 2 s.

concentration of particles at the bottom of the pipe is higher than that at the top. To quantify the size segregation after the bend, the possible size segregation at the inlet is neglected.

A typical case in the experimental work by Lee et al.¹⁰ is chosen as the base case for the present simulation, and the parameters used for the base case are listed in Table 2. The damping constant there corresponds to a restitution coefficient 0.4. Note that, to be computationally feasible, the base case corresponds to the one using coarse particles in their work. The particles are assumed to be spherical, with their sizes varying uniformly in the range listed in Table 2. The parameters for DEM simulation listed have been used in other studies dealing with glass beads.^{15,31,36}

3. Key Flow Features

In this section, the numerical results of gas–solid flow in bends are examined against some key features observed in physical experiments in the literature. The features considered include rope formation and dispersion, particle segregation, particle velocity reduction, and particle recirculation. Because the conditions for the present simulation and the experimental

work in the literature are not same, the analysis in this work is mainly qualitative.

Roping is the most notable feature in the gas–solid flow in a bend and characterized by the phenomenon that most of particles are close to the outer wall of the bend and there are very few particles close to the inner wall. It has been extensively studied in the literature since it causes segregation and uneven feeding.^{5,7,10,20} Generally speaking, a rope is formed because of the inertia and inelastic collision between particles and between particles and wall. As shown in Figure 2, this phenomenon can be captured by the present CCDM and a rope forms in the bend section and disperses after the plane of $Z/D = 4$ along the vertical section of the bend.

Figure 4 shows the porosity distribution at different times. It can be seen from Figure 4a–c that the rope is unsteady since the value and position of the maximum particle concentration change with time. At $t = 1.0$ s, the value of the maximum particle concentration ($= 1 - \text{porosity}$) is lower than those at $t = 1.5$ and 2.0 s, and the position of the maximum particle concentration is not as obvious as those at $t = 1.5$ and 2.0 s.

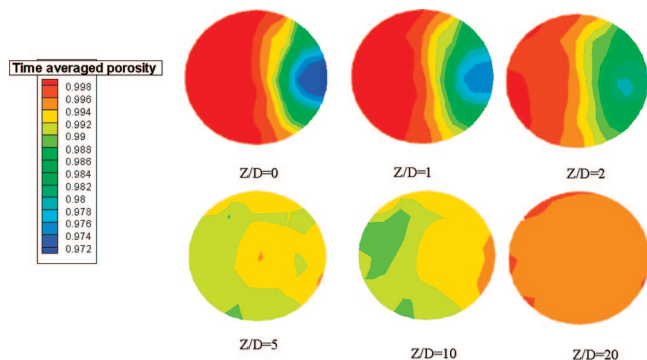


Figure 5. Time-averaged spatial distribution of porosity at different cross sections of the vertical pipe of the bend in the base case.

As shown in Figure 4d, the distribution of time-averaged porosity is smoother than those at different times.

The particle concentration in the rope at different cross sections can be used to quantify the segregation problems caused by roping. Figure 5 shows the profile of particle concentration at different cross sections in the vertical pipe. At $Z/D = 0$, a rather concentrated rope is close to the outer wall. At $Z/D = 2$, the maximum concentration has shifted toward the center of the pipe. At $Z/D = 5$ and 10, the maximum concentration has shifted to the region close to the inner wall. At $Z/D = 20$, the rope is dispersed and the concentration profile of particles is almost uniform. This trend qualitatively agrees with the experimental observation by Huber and Sommerfeld.⁵ The shift of the maximum concentration is due to the change of gas flow field and the collision between particles in the rope, as will be discussed in the next section. As mentioned earlier, the shift of the region of high particle concentration from the outer wall to the middle of the pipe is not satisfactorily predicted in the previous simulations.^{8,9}

It is reported that particle velocity will decrease considerably at a bend and the afterward acceleration causes additional pressure loss.⁴¹ This behavior is also captured in the present simulation and shown in Figure 3. Quantitatively, the particle velocity is ~ 7 m/s at the bend inlet but reduced to ~ 3.5 m/s at the bend exit.

When the superficial gas velocity is low (10.6 m/s in this case), Rao et al.⁴² observed that some particles recirculate in the area close to the inner wall of a bend. This phenomenon is largely reproduced in the present simulation. As shown in Figure 6, there are some particles flowing downward along the inner

wall of the bend and then flowing upward along the middle of the bend. Those circulating particles have a longer residence time than other particles. The reason for this phenomenon is because the gas velocity in the area close to the inner wall at the bend exit is much lower than that close to the outer wall giving a low gas–particle interaction force there, as will be discussed in the next section.

To further examine the capability of the present CCDM approach, a simulation has been made with a bend that is more smooth in bend shape by changing the bend radius to pipe diameter ratio. The parameters of gas phase and particle phase are the same as those in the base case except that small particles with a uniform particle size distribution in a range of 0.38–0.62 mm are used. From Figures 3 and 7 it can be seen that the rope in the smooth bend disperses much slower than in the sharp bend (i.e., the base case). Also, particle segregation in the smooth bend is more obvious than that in the sharp bend. Larger particles are close to the outer wall while smaller ones are close to the inner wall. The phenomena are qualitatively similar to those observed in the experiments.^{5,7} Yilmaz and Levy⁹ also observed that a rope can disperse quicker in a sharp bend than in a smooth bend. These investigators also attempted but failed to model the behavior by the LPT method.

4. Analysis of the Interaction Forces

Forces between gas and particles, between particles, and between particles and wall are the key factors responsible for the features of gas–solid two-phase flow in a bend. They are difficult to obtain by the TFM and LPT modeling. Actually, as discussed above, some of the key features can not be captured by these approaches. The forces are difficult to measure experimentally at this stage of development. However, they can be readily obtained by the present CCDM. In this section, the forces will be analyzed to understand their roles in governing the flow in a pneumatic conveying bend.

4.1. Gas–Particle Interaction Force. Gas–particle interaction force in a bend will affect the motion of both gas and solid phases. On one hand, the effect of gas on particles is mainly through the drag force, which is the dominant force governing the motion of particles in pneumatic conveying. On the other hand, the presence of solid phase will change the permeability distribution in the bed and hence can change the velocity and pressure distributions of gas phase. In this work, the effect of particle phase on gas flow is obtained and divided into two parts.

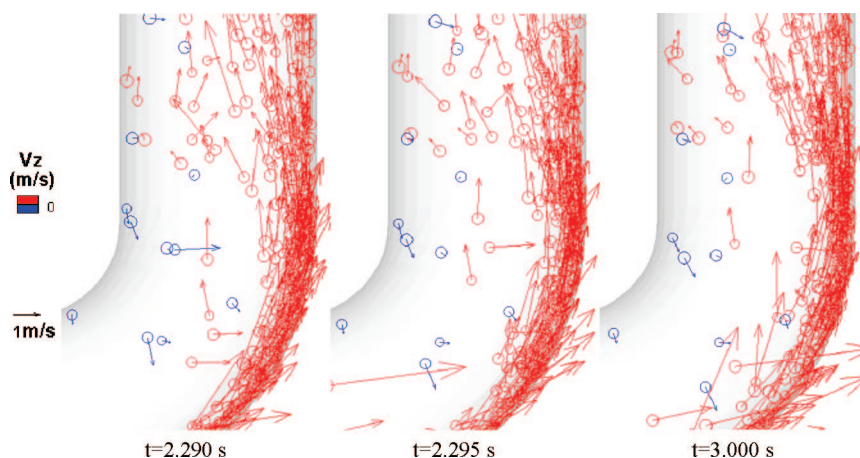


Figure 6. Downward flow of some particles around the inner wall of the bend when the superficial gas velocity is 10.6 m/s, which is lower than that in the base case. Arrows represent particle velocity vectors and color represents particle axial velocity.

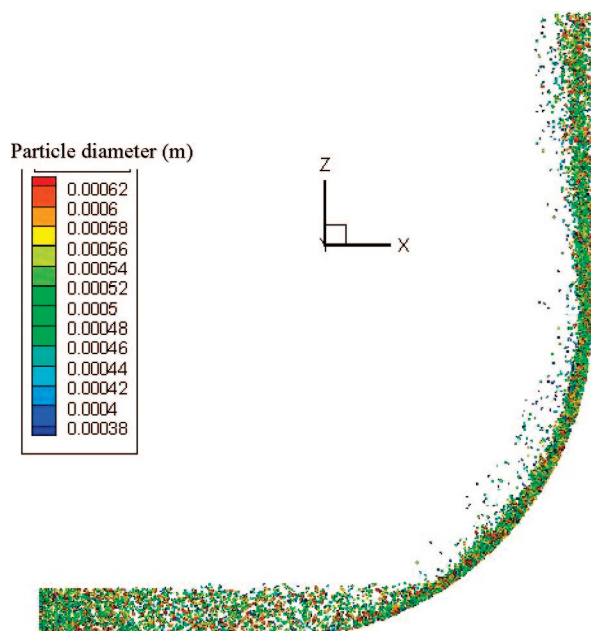


Figure 7. Rope formation and particle size segregation in a smooth bend of the full conveying pipe (the ratio of bend radius to pipe diameter equals 5).

The first is the effect on the axial velocity, and the other is the effect on the radial and tangential velocities, which are related to the secondary flow in bends.

Figure 8 shows the effect of the presence of particles on the axial velocity of gas phase in the bend considered. There is a maximum axial velocity whose position at $Z/D = 1$ is close to the outer wall for pure gas flow (Figure 8a) because of the effect of inertia and close to the center of the pipe for gas–solid flow (Figure 8b). It can be seen from Figure 8 c that the gas–solid interaction force, i.e., the resistant force from particles to gas flow, reaches its maximum in the region where the peak of the axial velocity shifts. This shift is believed to be caused by the resistant force. Gas tends to flow through the region where the resistant force is small. The occurrence of the region with a large gas–solid interaction force or resistant force can be explained as follows. In this region, gas velocity is ~ 15 m/s (Figure 8) and particle velocity is ~ 3.5 m/s (Figure 20). So the relative velocity between two phases is ~ 11.5 m/s. According to the equations in Table 1, the drag force on a particle will be large when the relative velocity between phases is large. That is, the gas–solid interaction force will be large since the gas–solid interaction force is the sum of the drag forces.

The other part, as shown in Figure 9, is the effect of the presence of solid phase on the secondary flow of gas phase, which is important since the secondary flow has been thought as one of the main reasons for the dispersion of particle ropes. Yilmaz and Levy⁹ have reported this effect by use of the LPT method. The present simulation results are similar to theirs for single-phase flow, but there are two main differences for two-phase flow. First, they showed that the secondary flow within the rope under the two-phase flow conditions is random and gas may even reverse its flow direction. However, in our simulation, the gas flow within the rope is neither random nor with reversed direction but just decreases compared to the single-phase flow. Second, they showed that the velocity of the secondary flow along the side wall is smaller than that in the single-phase flow. But the present results suggest that the velocity along the

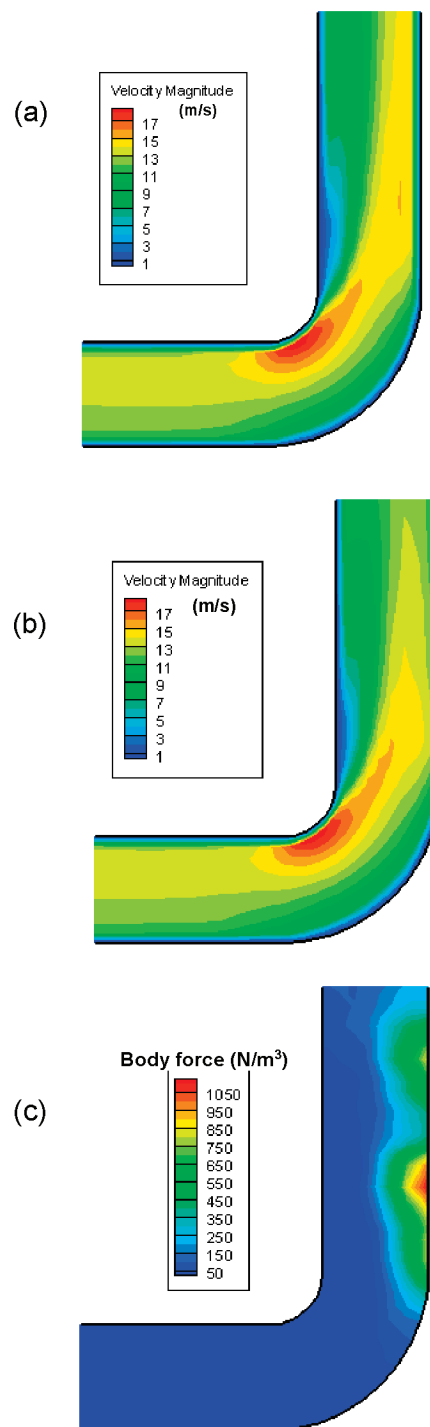


Figure 8. Front view of axial velocity and gas–solid interaction force distribution at the B–B section (defined in Figure 18) in the base case (Figure 1): (a) gas velocity of single-phase flow; (b) gas velocity of gas–particle flow at $t = 2$ s; and (c) gas–solid interaction force in the axial direction at $t = 2$ s.

side wall in two-phase flow is larger. The differences of the secondary flow in flows are also thought to be caused by the large gas–solid interaction force region, which is close to the outer wall at the bend exit (Figure 8c). Large gas–solid interaction force within the rope makes less gas flow through the rope and consequently more gas flow along the side wall from the outer wall to the inner wall, which in turn moves particles inside the rope to the inner wall of the pipe along the side walls. The random flow obtained from the LPT simulation is possibly caused by the fact that the calculation

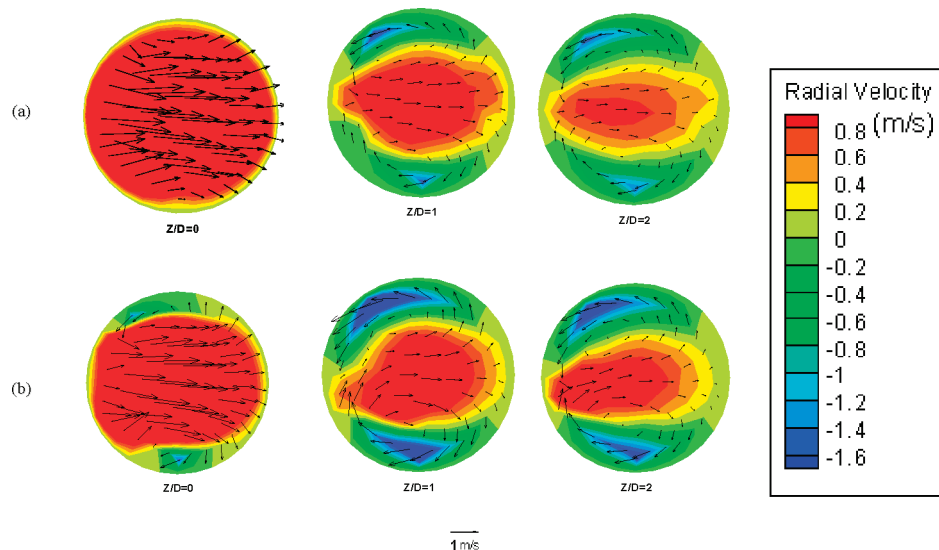


Figure 9. Secondary flow fields at different cross sections of the vertical pipe of the bend in the base case: (a) single-phase flow solution; (b) gas-particle flow solution at $t = 2$ s (arrows represent the gas velocity vectors).

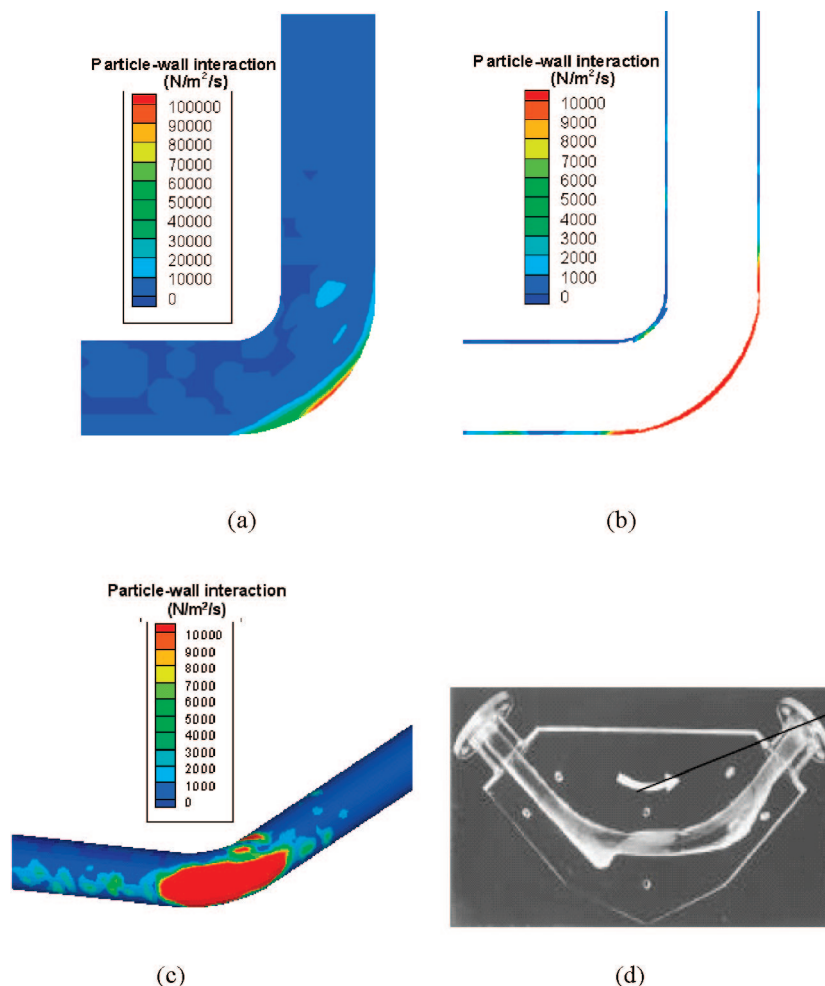


Figure 10. Spatial distribution of particle-wall TACI for the base case: (a) front view; (b) at the B-B section (defined in Figure 18); (c) at outer wall of the bend; (d) an experimental bend of solid clear acrylic, worn by the passage of alumina particles.⁵⁰

of the volume fraction of solid phase in LPT is not accurate enough since the interaction between particles is ignored. The difference may also originate from the fact that the simulation conditions are different. Further study is probably necessary to clarify this issue.

4.2. Particle-Wall Interaction Force. Particle-wall interaction force in bends attracts many research efforts since it closely relates to the wearing of transport pipes and the degrading of the conveyed product.^{1,3,43–45} In general, for a given bend, the extent of erosion on the wall depends on

three factors: operational conditions, nature of target materials, and properties of impact particles. Of these factors, operational conditions, such as impinging velocity, impact angle, particle number density at impact, and properties of the carrier fluid, are the most important.^{1,45,46} For dilute flow, Stokes number can be used to evaluate the impactability of

particles on wall. For dense flow, the situation is more complicated because the collision between particles can form a shield to impede particle–wall collision.^{44,47} The present simulation indeed indicates that particle–particle collision can cause some particles to collide with the wall many times but at the same time some particles do not necessarily collide directly with the wall but the shielding effect.

In this work, the particle–wall interaction is quantified by use of the so-called time-averaged collision intensity (TACI), which is related to wear,⁴⁸ defined by

$$\text{TACI} = \frac{\sum_{t=0}^T \sum_{i=1}^{k_m} |\mathbf{f}_{cn,i} + \mathbf{f}_{dn,i} + \mathbf{f}_{ct,i} + \mathbf{f}_{dt,i}|}{A \times T} \quad (5)$$

where A is the surface area of a sample wall, T is the simulation time or sampling time, and k_m is the number of particles contacting with the sample wall at a given time. Physically, it can be understood as the particle–wall interaction forces per unit (wall surface) area per unit time.

Figure 10 shows the distribution of TACI between particles and wall for the base case. From Figure 10a, it can be seen that the area with the highest TACI is slightly lower than that of the center of the horizontal pipe. This is because at that height both the particle concentration and velocity from the horizontal pipe are high, which results in high

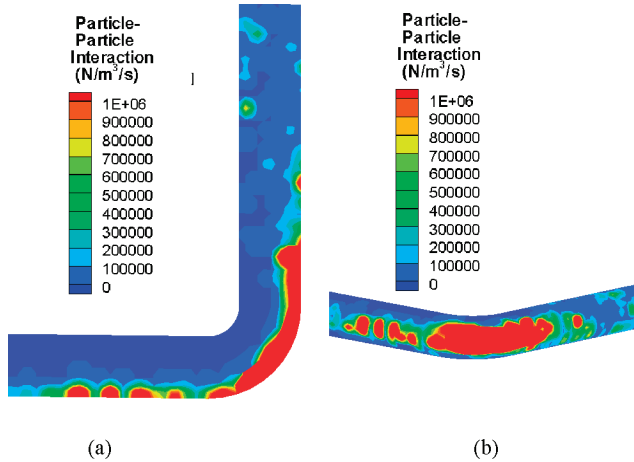


Figure 11. Spatial distribution of particle–particle TACI, averaged over 2 s for the base case: (a) at the B–B section (defined in Figure 18); (b) bottom view of the bend region.

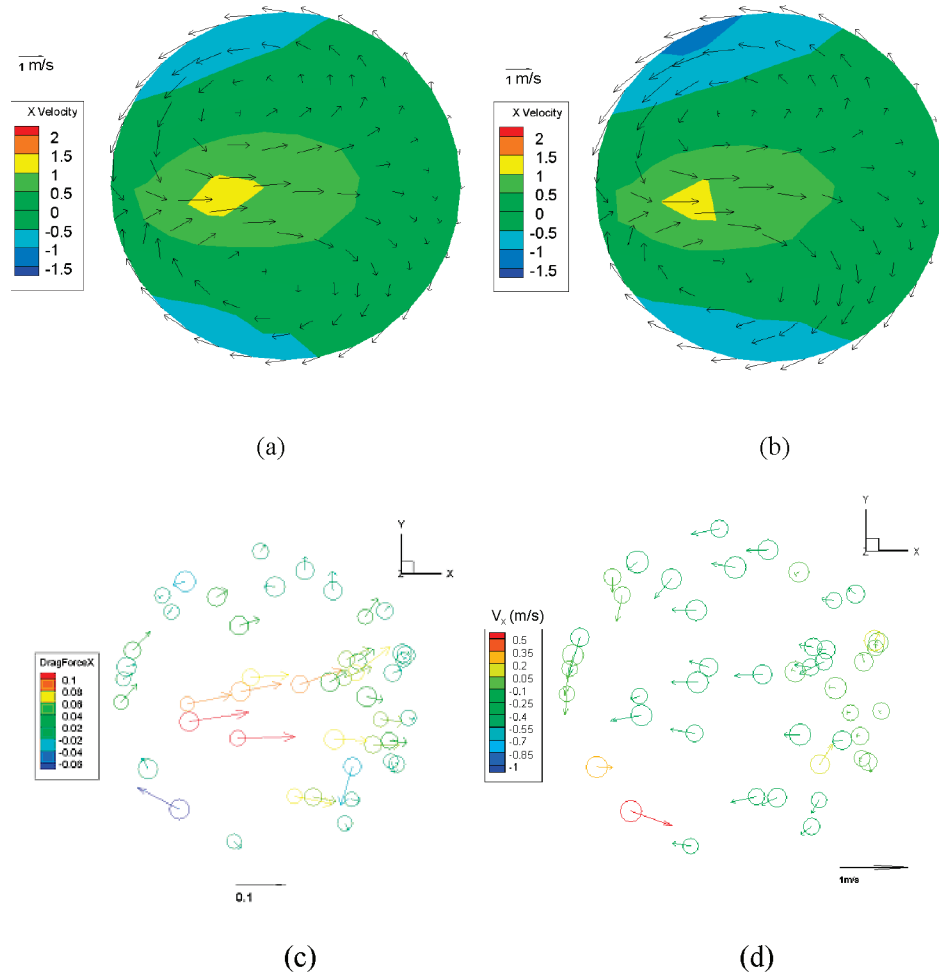


Figure 12. Comparison of gas velocity, gas–particle force and particle velocity distribution in the post bend region at $t = 2$ s: (a) and (b) vectors of the secondary flow of gas phase at cross section of $Z/D = 4.5$ and $Z/D = 5$ respectively, colored by gas velocity in the x -direction; (c) the radial and tangential components of the forces on particles between sections $Z/D = 4.5$ and $Z/D = 5$, colored by the force in the x -direction and normalized by dividing particle gravity; and (d) the radial and tangential velocities of particles between sections $Z/D = 4.5$ and $Z/D = 5$, colored by the particle velocity in the x -direction.

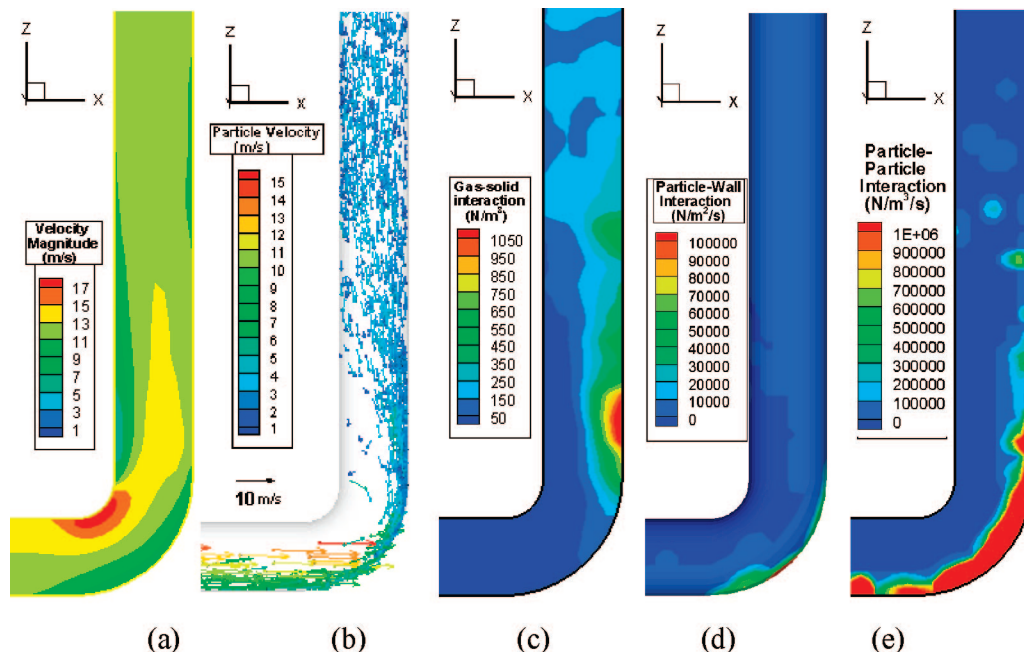


Figure 13. Spatial distributions of (a) gas velocities at the B-B section (defined in Figure 1) at $t = 2$ s; (b) particle velocities in the whole bend at $t = 2$ s; (c) gas-particle interaction force at B-B section at $t = 2$ s; (d) front view of the particle-wall TACI averaged over 2 s; and (e) particle-particle TACI averaged over 2 s at the B-B section when the solid mass flow rate is 46.3 kg/s (increased from 31.1 kg/s for the base case).

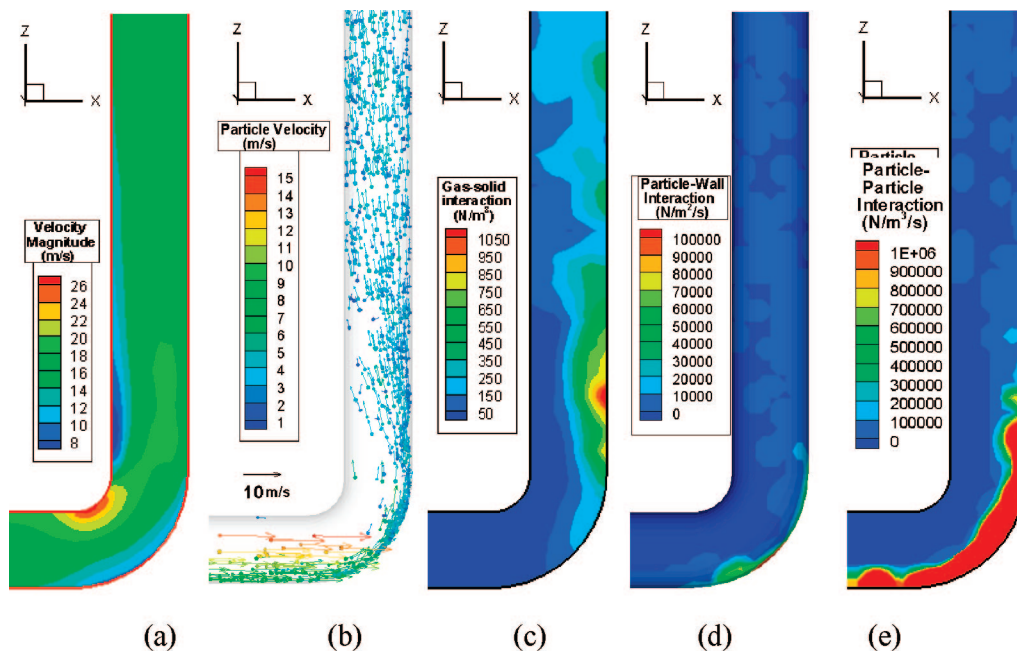


Figure 14. Spatial distributions of (a) gas velocities at the B-B section (defined in Figure 1) at $t = 2$ s; (b) particle velocities in the whole bend at $t = 2$ s; (c) gas-particle interaction force at B-B section at $t = 2$ s; (d) front view of the particle-wall TACI averaged over 2 s; and (e) particle-particle TACI averaged over 2 s at the B-B section when the gas velocity is 16.0 m/s (increased from 11.9 m/s for the base case).

collision velocities and frequency in a bend. At the top of the horizontal pipe, the particle velocity is high but the concentration of particle is low, so the TACI is just at a medium level. At the bottom of the horizontal pipe, the particle concentration is high but the velocity is low, so the TACI is also at a medium level. This proves that the most intensive particle-wall interaction position depends on not only the particle velocity but also on the particle concentration. This is reasonable as it is consistent with the common sense. So the concept of TACI can be used to locate the pipe wall position that experiences the highest particle-wall

interaction and can be first worn out. From Figure 10b it can be seen that some particles also collide with the inner wall when Z/D is greater than 1.

The computational results of the spatial distribution of bend wall erosion have also been compared with the experimental results as shown in Figure 10c and d. It can be seen that they qualitatively agree with each other. Clearly, the present simulation results indicate that the magnitude of the particle-wall interaction forces due to collision and the frequency of collisions are important parameters for

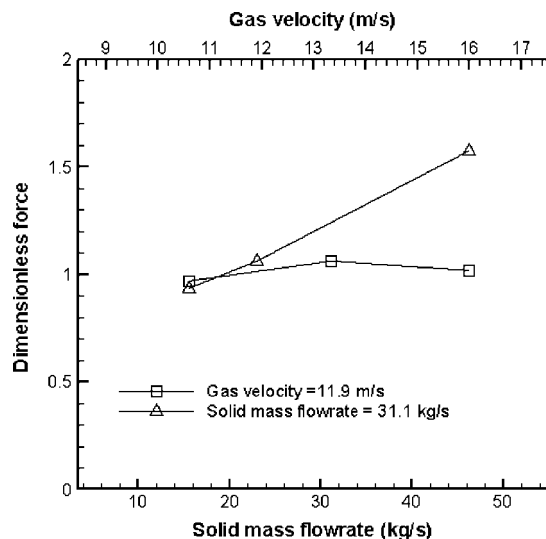


Figure 15. Time-averaged gas-particle interaction force as a function of solid flow rate or gas velocity.

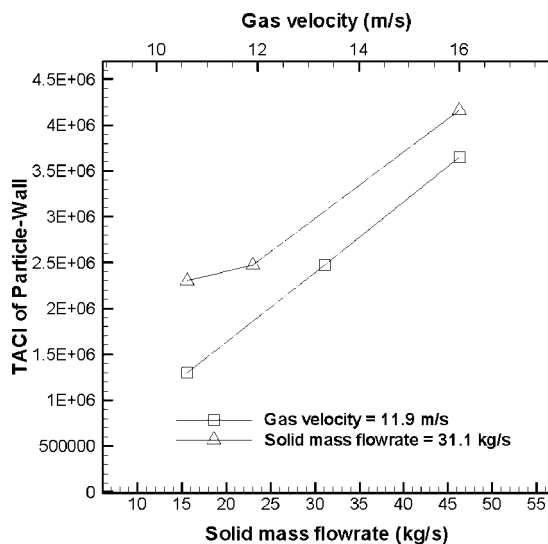


Figure 16. Particle-wall TACI as a function of solid flow rate or gas velocity.

particle-wall erosion prediction. The particle-wall interaction will also affect the flow of particles as discussed below.

4.3. Particle-Particle Interaction Force. Particle-particle interaction force is important since it directly relates to particle attrition and wall erosion.^{44,47} For convenience, it is quantified in a way similar to the concept of TACI defined in eq 5. However, area A in the equation is replaced by volume to give the interaction between particles per unit volume per unit time. In the calculation, this is done by dividing the bend, i.e., the computational domain, into many small elements and TACI is calculated for each element.

There are two interesting findings about the interparticle collision. First, the spatial distribution of the particle-particle TACI is similar to that of the particle-wall collision (Figure 10 vs. Figure 11). In particular, the region for high particle-particle TACI is linked to the region that gives high particle-wall TACI at the outer bend wall. This suggests that particle-wall collision can lead to particle-particle collision in regions close to a bend wall. It is because some particles, after colliding with the bend wall, will change their velocities and directions, and collide with incoming particles, forming a shielding layer as mentioned earlier.

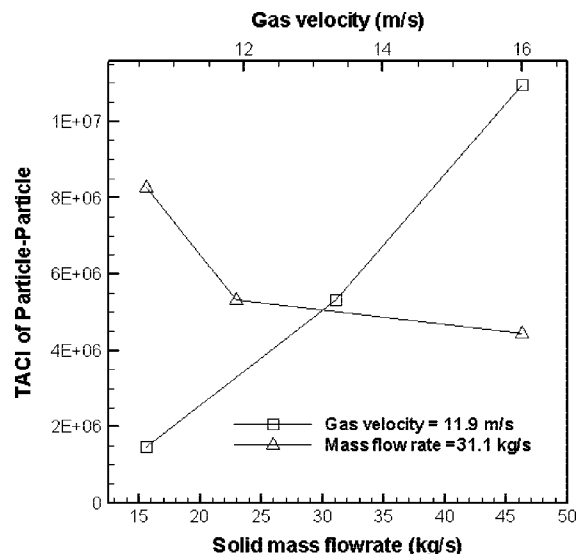


Figure 17. Particle-particle TACI as a function of solid flow rate or gas velocity.

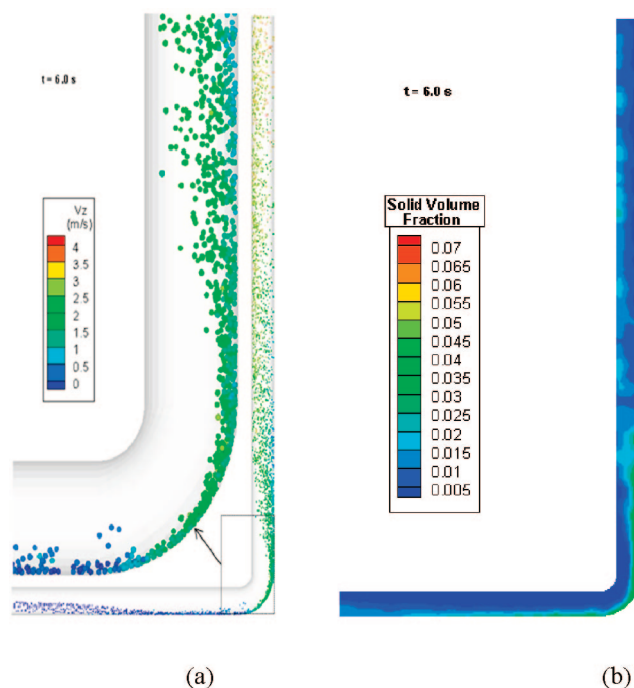


Figure 18. Spatial distributions of (a) particle positions and velocities and (b) particle concentration when the initial particle velocity is 3 m/s.

Second, it is found that not only the secondary flow but also the particle-particle collision contribute to the dispersion of a rope. The mechanism of rope dispersion because of particle-particle collision can be explained by use of the information shown in Figures 12. This figure shows the secondary flow of gas phase, the radial and tangential drag forces, and the radial and tangential particle velocities at sections from $Z/D = 4.5$ to $Z/D = 5$. From Figures 12a, b, and c it can be seen that the radial and tangential drag force distribution accords with the secondary flow field. At the center, the gas flows from the inner wall to the outer wall and the direction of the drag force on the particles at the center is also from the inner to outer wall. However, Figure 12d shows that the particles at the center move in the direction opposite to the direction of the gas phase and drag forces. The results indicate that it is the particle-particle collision that makes the particles in the rope move to the inner wall of the pipe

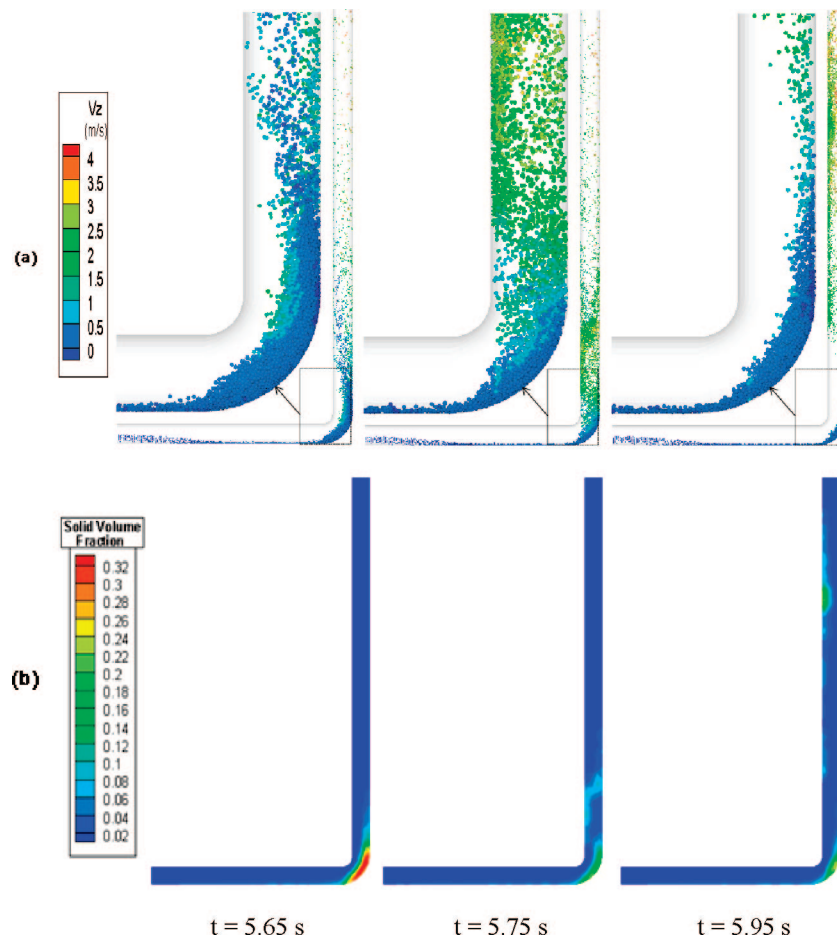


Figure 19. Spatial distributions of (a) particle positions and velocities and (b) particle concentration at different times when the initial particle velocity is 2 m/s.

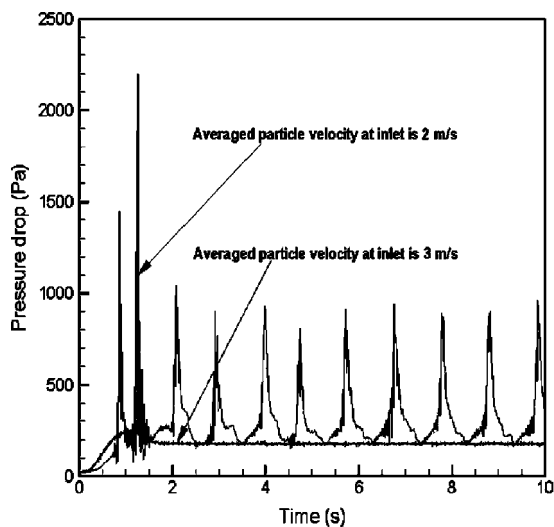


Figure 20. Variation of the pressure drop in the bend with time for different initial particle velocities.

through the center of the pipe. New coming particles may collide with the existing ones along the wall, and change their flow direction, moving from the outer wall to the inner wall. This movement can lead to rope dispersion.

5. Effects of Inlet Conditions

The gas–solid flow in pneumatic conveying bends is affected by a range of variables related to operational conditions, particle

characteristics and properties, and pipe properties and geometry.^{1,2,10,49} The results presented above are just related to one given flow condition. It is of interest to know how the flow depends on the relevant variables. The CCDM model presented offers a method to achieve this aim. But this requires a systematic study that has to be done in the future. Nonetheless, as an example to demonstrate the capability of the proposed approach, the effects of inlet conditions have been studied as part of the present work. This is done by conducting a number of simulations by varying gas flow rate, solid flow rate, or particle velocities at the inlet while other variables are fixed at their base values listed in Table 2.

Figures 13 and 14 show the spatial distributions of gas velocity, solid flow pattern and velocity, and interaction forces between gas, solid, and wall when respectively changing the solid and gas flow rates. Comparing the results with those shown in Figures 3, 8, 10, and 11 indicates that the key features in these spatial distributions are similar to each other. The results confirm that the findings about the flow features and the roles of the gas–particle, particle–particle, and particle–wall interaction forces, as elucidated above, are qualitatively valid.

However, quantitatively, the magnitudes of these interaction forces vary with the gas and solid flow rates, as shown in Figures 15–17. Here, the gas–solid interaction is quantified by use of an averaged and normalized gas–particle interaction force at a given time, which is calculated by $(1/n)\sum_{i=1}^n (|f_{pf,i}|/m_i g)$, where n is the total number of particles in the system considered. Gas–particle interaction force may vary with time since the flow is unsteady. Thus, the concept of time-averaged gas–particle

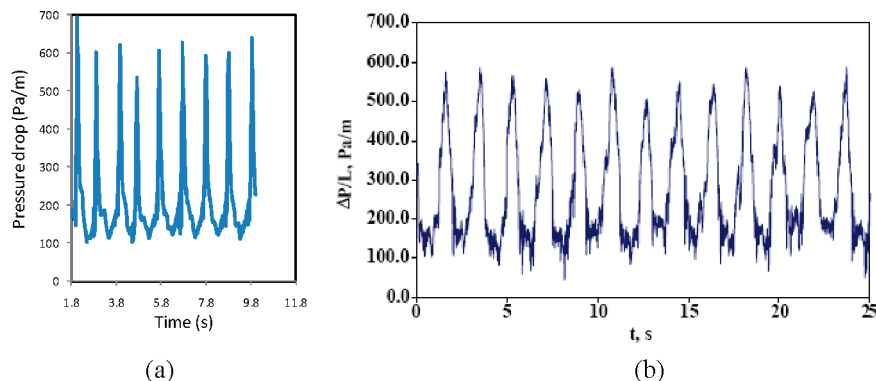


Figure 21. Pressure fluctuation (corresponding to the case with initial particle velocity of 2 m/s in Figure 20): (a) simulated; (b) measured.¹⁰

force is used, done by averaging the forces at different sample times over 1 s (from $t = 2$ to $t = 3$ s in this case). Figure 15 shows that this time-averaged force does not change much with solid flow rate but increases with gas velocity. According to the equation to calculate the gas–particle interaction force in Table 1, the magnitude of gas–particle interaction force is proportional to the squared relative velocity between gas and particles. The increase of gas velocity will increase the relative velocity while the increase of solid flow rate will not increase the relative velocity much; hence, the gas and solid flow rates give different effects on gas–particle interaction force.

Figure 16 shows that the time-averaged particle–wall TACI increases with solid flow rate or gas velocity. This can be explained by the fact that the increase of solid flow rate will increase the number of particle–wall interactions in a given time period and the increase of gas velocity will increase particle velocities leading to higher impact energy on the wall. For the particle–particle interaction, as shown in Figure 17, an interesting finding is that the particle–particle TACI decreases as gas velocity increases. This is because a higher gas velocity will shorten the residence time of particles and consequently reduce the total number of particles in the system and the number of particle–particle interactions in a given time period.

Under the present simulation settings, when we change solid mass flow rate, we just control the number of particles generated at the inlet in a given period of time. At the same time, we can also change the velocities of particles at the inlet, here referred to as the initial particle velocity for convenience. Note that when solid mass flow rate is fixed, the lower the initial particle velocity, the higher is the solid concentration. To examine the effect of the initial particle velocity, simulations were conducted when the other conditions corresponded to the base case. In particular, emphasis was given to the situation when the average initial particle velocity was low to yield a more dense flow. Figures 18 and 19 show that the initial particle velocity affects particle concentration distribution significantly. When the initial velocity was decreased from 3 (Figure 18) to 2 m/s (Figure 19), the highest solid concentration in the bend region increased from 0.07 to 0.32. Moreover, as shown in Figure 19, the flow became unstable when the initial particle velocity was 2 m/s. It was observed that particles accumulated from the outer wall of the bend to some extent, and then the accumulated particles were dragged upward by gas batch by batch. This accumulation–dragging away pattern happened periodically. Corresponding to this pattern is the large periodic fluctuation in the pressure drop of the bend as shown in Figure 20. Note that the pressure drop is almost constant after the initial stage (~ 1 s) when the initial particle velocity is 3 m/s. The results suggest that the flow in a bend is more stable if particles are accelerated before entering

the bend. The acceleration may be achieved by narrowing the cross area of the pipe. The effectiveness of this treatment will be examined in the future.

Lee et al.¹⁰ did observe a large pressure fluctuation in their experiment. Figure 21 shows the comparison between the simulated and measured pressure drops. It can be seen that the two results are qualitatively comparable. Quantitatively there is a noticeable difference here: the period of fluctuations in the simulation is shorter than that in the measurement although the magnitude of fluctuations is close enough. On the other hand, as noted earlier, the conditions for numerical experiments do not fully match those for physical experiments. The difference observed is therefore understandable. Nonetheless, the qualitative agreement between physical and numerical studies, in pressure drop fluctuation, and other aspects discussed in section 3 provides some confidence about the reliability of the present numerical approach, which, at this stage of development, is mainly to develop know-why rather than know-how knowledge.^{51,52}

6. Conclusions

The CCDM approach has been extended from two- to three-dimensions to study the gas–solid flow in pneumatic conveying bends. It is shown that the approach can satisfactorily capture the key features of the gas–solid flow in this system such as roping, particle segregation, particle velocity reduction, particle recirculation, and pressure fluctuation. The analysis of the gas–particle, particle–wall, and particle–particle interaction forces leads to the following conclusions:

(1) The effect of solid phase on gas phase is obvious and should not be ignored. With the increase of solid load, the peak of gas axial velocity shifts from the outer wall toward the inner wall at a bend exit. The reason for the shift is that the volumetric gas–particle interaction force in the outer wall region is higher than that in the inner wall region. Correspondingly, the so-called secondary flow is suppressed in the outer wall region but enhanced along the side wall at the bend exit. The shift of the peak of gas axial velocity and the secondary flow both contribute to the dispersion of a rope.

(2) The wear pattern in a bend depends on the magnitude of the interaction forces and the frequency of interactions between particles and wall and can be located from the spatial distribution of the time-averaged particle–wall collision intensity. Strong particle–wall interactions exist in the outer wall of a bend, which can lead to strong particle–particle interactions. Particle–wall and particle–particle interactions both contribute to the dispersion of a rope.

(3) The spatial distributions of interaction forces between gas and particles, between particles and wall, and between particles

show similar trends for different gas and solid flow rates. However, the magnitudes of those interactions vary. The gas–particle interaction does not change much with solid flow rate but increases with gas velocity. The particle–wall interaction becomes more intensive when solid flow rate or gas velocity is increased. The particle–particle interaction increases with solid flow rate but decreases with gas velocity.

(4) The velocities of particles at the inlet of a bend are also an important variable affecting the gas–solid flow patterns in the bend. If the particle velocity is too low, unstable solid flow may result. This is an issue that needs much intensive study in the future under conditions more relevant to practical conveying systems.

Finally, it should be pointed out that the present study is largely preliminary, aiming to extend and examine the capability of the CCDM model when applied to pneumatic conveying bends. More detailed, systematic studies are necessary in order to understand the effects of variables related to operational conditions, particle characteristics and properties, and pipe properties and geometry and generate results useful to engineering application.

Acknowledgment

The authors are grateful to the Australia Research Council (ARC) for the financial support of this work.

Nomenclature

A = area, m^2
 c = damping coefficient, dimensionless
 c_{d0} = fluid drag coefficient, dimensionless
 d = particle diameter, m
 E = Young's modulus, Pa
 f_c = contact force, N
 f_d = damping force, N
 f_{pf} = particle–fluid interaction force, N
 F = volumetric force, N/m^3
 g = gravity acceleration vector, 9.81 m/s^2
 G = gravity vector, N
 G_s = solid mass flow rate, $kg/(m^2 \text{ s}^1)$
 I = moment of inertia of a particle, $k \text{ gm}$
 k_c = number of particles in a computational cell, dimensionless
 k_i = number of particles in contact with particle i , dimensionless
 k_m = number of contacts in a sample, dimensionless
 m = mass of a particle, kg
 M = rolling friction torque, N m
 n = number of particles in a considered system, dimensionless
 n = unit vector in the normal direction of two contact spheres, dimensionless
 P = pressure, Pa
 Δp = pressure drop, Pa
 R = radius vector (from particle center to a contact point), m
 R = magnitude of R , m
 Re = Reynolds number, dimensionless
 A = the area of wall in a local cell, m^2
 t = time, s
 T = total simulation time, s
 T = driving friction torque, N m
 u = fluid velocity, m/s
 V = volume, m^3
 V = velocity vector, m/s
 ΔV_c = volume of a computational cell, m^3

Greek Letters

α_s = solids concentration, dimensionless
 β = empirical coefficient defined in Table 2, dimensionless

δ = vector of the particle–particle or particle–wall overlap, m
 δ = magnitude of δ , m
 ε = porosity, dimensionless
 μ = fluid viscosity, $kg/m \cdot s$
 μ_r = coefficient of rolling friction, m
 μ_s = coefficient of sliding friction, dimensionless
 ν = Poisson's ratio, dimensionless
 ρ = density, kg/m^3
 τ = viscous stress tensor, N/m^2
 ω = angular velocity, rad/s
 ω = magnitude of angular velocity, rad/s
 $\hat{\omega}$ = unit angular velocity
Subscripts
 c = contact
 d = damping
 D = drag
 f = fluid phase
 ij = between particle i and j
 $i(j)$ = corresponding to $i(j)$ th particle
 max = maximum
 n = in normal direction
 p = particle phase
 $p-p$ = between particle and particle
 $p-w$ = between particle and wall
 t = in tangential direction

Literature Cited

- (1) Fan, J. R.; Yao, J.; Cen, K. F. Antierosion in a 90 degrees bend by particle impaction. *AIChE J.* **2002**, *48* (7), 1401–1412.
- (2) Bilirgen, H.; Levy, E. K. Mixing and dispersion of particle ropes in lean phase pneumatic conveying. *Powder Technol.* **2001**, *119* (2–3), 134–152.
- (3) Mills, D.; Mason, J. S. Particle concentration effects in bend erosion. *Powder Technol.* **1977**, *17* (1), 37–53.
- (4) Kliafas, Y.; Holt, M. LDV measurements of a turbulent air-solid 2-phase flow in a 90-degree bend. *Exp. Fluids* **1987**, *5* (2), 73–85.
- (5) Huber, N.; Sommerfeld, M. Characterization of the cross-sectional particle concentration distribution in pneumatic conveying systems. *Powder Technol.* **1994**, *79* (3), 191–210.
- (6) Tu, J. Y.; Fletcher, C. A. J. Numerical computation of turbulent gas-solid particle flow in a 90-degrees bend. *AIChE J.* **1995**, *41* (10), 2187–2197.
- (7) Levy, A.; Mason, D. J. The effect of a bend on the particle cross-section concentration and segregation in pneumatic conveying systems. *Powder Technol.* **1998**, *98* (2), 95–103.
- (8) Huber, N.; Sommerfeld, M. Modelling and numerical calculation of dilute-phase pneumatic conveying in pipe systems. *Powder Technol.* **1998**, *99* (1), 90–101.
- (9) Yilmaz, A.; Levy, E. K. Formation and dispersion of ropes in pneumatic conveying. *Powder Technol.* **2001**, *114* (1–3), 168–185.
- (10) Lee, L. Y.; Quek, T. Y.; Deng, R. S.; Ray, M. B.; Wang, C. H. Pneumatic transport of granular materials through a 90 degrees bend. *Chem. Eng. Sci.* **2004**, *59* (21), 4637–4651.
- (11) Lim, E. W. C.; Wang, C. H.; Yu, A. B. Discrete element simulation for pneumatic conveying of granular material. *AIChE J.* **2006**, *52* (2), 496–509.
- (12) Yu, A. B.; Xu, B. H. Particle-scale modelling of gas-solid flow in fluidisation. *J. Chem. Technol. Biotechnol.* **2003**, *78* (2–3), 111–121.
- (13) Xu, B. H.; Yu, A. B. Numerical simulation of the gas-solid flow in a fluidized bed by combining discrete particle method with computational fluid dynamics. *Chem. Eng. Sci.* **1997**, *52* (16), 2785–2809.
- (14) Tsuji, Y.; Tanaka, T.; Ishida, T. Lagrangian numerical-simulation of plug flow of cohesionless particles in a horizontal pipe. *Powder Technol.* **1992**, *71* (3), 239–250.
- (15) Feng, Y. Q.; Yu, A. B. Assessment of model formulations in the discrete particle simulation of gas–solid flow. *Ind. Eng. Chem. Res.* **2004**, *43* (26), 8378–8390.
- (16) Cundall, P. A.; Strack, O. D. L. Discrete numerical-model for granular assemblies. *Geotechnique* **1979**, *29* (1), 47–65.
- (17) Deen, N. G.; Annaland, M. V. S.; Van Der Hoef, M. A.; Kuipers, J. A. M. Review of discrete particle modeling of fluidized beds. *Chem. Eng. Sci.* **2007**, *62*, 28–44.

- (18) Zhu, H. P.; Yu, A. B. Averaging method of granular materials. *Phys. Rev. E* **2002**, *66* (2).
- (19) Zhu, H. P.; Yu, A. B. Micromechanic modeling and analysis of unsteady-state granular flow in a cylindrical hopper. *J. Eng. Math.* **2005**, *52* (1), 307–320.
- (20) Akilli, H.; Levy, E. K.; Sahin, B. Gas-solid flow behavior in a horizontal pipe after a 90 degrees vertical-to-horizontal elbow. *Powder Technol.* **2001**, *116* (1), 43–52.
- (21) Kawaguchi, T.; Tanaka, T.; Tsuji, Y. Numerical analysis of density wave in dense gas-solid flows in a vertical pipe. *Prog. Theor. Phys. Suppl.* **2000**, (138), 696–701.
- (22) Xiang, J. S.; McGlinchey, D. Numerical simulation of particle motion in dense phase pneumatic conveying. *Granular Matter* **2004**, *6* (2–3), 167–172.
- (23) Ouyang, J.; Yu, A. B. Simulation of gas-solid flow in vertical pipe by hard-sphere model. *Particulate Sci. Technol.* **2005**, *23* (1), 47–61.
- (24) Fraige, F. Y.; Langston, P. A. Horizontal pneumatic conveying: a 3d distinct element model. *Granular Matter* **2006**, *8* (2), 67–80.
- (25) Watano, S. Mechanism and control of electrification in pneumatic conveying of powders. *Chem. Eng. Sci.* **2006**, *61* (7), 2271–2278.
- (26) Han, T.; Levy, A.; Kalman, H. DEM simulation for attrition of salt during dilute-phase pneumatic conveying. *Powder Technol.* **2003**, *129* (1–3), 92–100.
- (27) Kuang, S. B.; Chu, K. W.; Yu, A. B.; Zou, Z. S.; Feng, Y. Q. Computational investigation of horizontal slug flow in pneumatic conveying. *Ind. Eng. Chem. Res.* **2008**, *47*, 470–480.
- (28) Li, J.; Webb, C.; Pandiella, S. S.; Campbell, G. M.; Dyakowski, T.; Cowell, A.; McGlinchey, D. Solids deposition in low-velocity slug flow pneumatic conveying. *Chem. Eng. Process.* **2005**, *44* (2), 167–173.
- (29) Xu, B. H.; Yu, A. B.; Chew, S. J.; Zulli, P. Numerical simulation of the gas-solid flow in a bed with lateral gas blasting. *Powder Technol.* **2000**, *109* (1–3), 13–26.
- (30) Feng, Y. Q.; Xu, B. H.; Zhang, S. J.; Yu, A. B.; Zulli, P. Discrete particle simulation of gas fluidization of particle mixtures. *AIChE J.* **2004**, *50* (8), 1713–1728.
- (31) Zhou, Y. C.; Wright, B. D.; Yang, R. Y.; Xu, B. H.; Yu, A. B. Rolling friction in the dynamic simulation of sandpile formation. *Physica A (Amsterdam)* **1999**, *269* (2–4), 536–553.
- (32) Mindlin, R. D.; Deresiewicz, H. Elastic spheres in contact under varying oblique forces. *J. Appl. Mech.: Trans. ASME* **1953**, *20* (3), 327–344.
- (33) Johnson, K. L. *Contact Mechanics*; Cambridge University Press: Cambridge, 1985.
- (34) Thornton, C.; Yin, K. K. Impact of elastic spheres with and without adhesion. *Powder Technol.* **1991**, *65* (1–3), 153–166.
- (35) Walton, O. R. Numerical-simulation of inclined chute flows of monodisperse, inelastic, frictional spheres. *Mech. Mater.* **1993**, *16* (1–2), 239–247.
- (36) Zhou, Y. C.; Yu, A. B.; Stewart, R. L.; Bridgwater, J. Microdynamic analysis of the particle flow in a cylindrical bladed mixer. *Chem. Eng. Sci.* **2004**, *59* (6), 1343–1364.
- (37) Di Felice, R. The voidage function for fluid particle interaction systems. *Int. J. Multiphase Flow* **1994**, *20* (1), 153–159.
- (38) Gidaspow, D., *Multiphase flow and fluidization*; Academic Press: San Diego, 1994.
- (39) Chu, K. W.; Yu, A. B. Numerical simulation of complex particle-fluid flows. *Powder Technol.* **2008**, *179* (3), 104–114.
- (40) Tsuji, Y.; Morikawa, Y. LDV measurements of an air solid 2-phase flow in a horizontal pipe. *J. Fluid Mech.* **1982**, *120* (JUL), 385–409.
- (41) McCluskey, D. R.; Easson, W. J.; Greated, C. A.; Glass, D. H. The use of particle image velocimetry to study roping in pneumatic conveyance. *Part. Part. Syst. Charact.* **1989**, *6* (3), 129–132.
- (42) Rao, S. M.; Zhu, K. W.; Wang, C. H.; Sundaresan, S. Electrical capacitance tomography measurements on the pneumatic conveying of solids. *Ind. Eng. Chem. Res.* **2001**, *40* (20), 4216–4226.
- (43) Deng, T.; Patel, M.; Hutchings, I.; Bradley, M. S. A. Effect of bend orientation on life and puncture point location due to solid particle erosion of a high concentration flow in pneumatic conveyors. *Wear* **2005**, *258* (1–4), 426–433.
- (44) Deng, T.; Chaudhry, A. R.; Patel, M.; Hutchings, I.; Bradley, M. S. A. Effect of particle concentration on erosion rate of mild steel bends in a pneumatic conveyor. *Wear* **2005**, *258* (1–4), 480–487.
- (45) Kalman, H. Attrition of powders and granules at various bends during pneumatic conveying. *Powder Technol.* **2000**, *112* (3), 244–250.
- (46) Salman, A. D.; Hounslow, M. J.; Verba, A. Particle fragmentation in dilute phase pneumatic conveying. *Powder Technol.* **2002**, *126* (2), 109–115.
- (47) Uemois, H.; Kleis, I. Critical analysis of erosion problems which have been little studied. *Wear* **1975**, *31* (2), 359–371.
- (48) Finnie, I. Some observations on erosion of ductile metals. *Wear* **1972**, *19* (1), 81.
- (49) Pan, R. Material properties and flow modes in pneumatic conveying. *Powder Technology* **1999**, *104* (2), 157–163.
- (50) Bradley, M., Understanding and controlling attrition and wear in pneumatic conveying. SHAPA Technical Paper No. 5, 1999.
- (51) Yu, A. B. Discrete element method—an effective method for particle scale research of particulate matter. *Eng. Comput.* **2004**, *21*, 205–214.
- (52) Zhu, H. P.; Yang, R. Y.; Zhou, Z. Y.; Yu, A. B. *Discrete simulation of particulate systems: theoretical developments*, *Chem. Eng. Sci.* **2007**, *62*, 3378–3396.

Received for review January 21, 2008

Revised manuscript received May 13, 2008

Accepted June 2, 2008

IE800108C